JOURNAL OF GEOPHYSICAL RESEARCH, VOL. 117, C04006, doi:10.1029/2011JC007649, 2012

Modeling winter circulation under landfast ice: The interaction of winds with landfast ice

Jeremy L. Kasper[1,2] and Thomas J. Weingartner[1]

Received 2 October 2011; revised 10 January 2012; accepted 11 February 2012; published 4 April 2012.

[1] Idealized models and a simple vertically averaged vorticity equation illustrate the effects of an upwelling favorable wind and a spatially variable landfast ice cover on the circulation beneath landfast ice. For the case of no along-shore variations in ice, upwelling favorable winds seaward of the ice edge result in vortex squashing beneath the landfast ice leading to (1) large decreases in coastal and ice edge sea levels, (2) cross-shore sea level slopes and weak ($<\sim$.05 m s^{-1}) under-ice currents flowing upwind, (3) strong downwind ice edge jets, and (4) offshore transport in the under-ice and bottom boundary layers of the landfast ice zone. The upwind under-ice current accelerates quickly within 2–4 days and then slows as cross-shore transport gradually decreases the cross-shore sea level slope. Near the ice edge, bottom boundary layer convergence produces ice edge upwelling. Cross-ice edge exchanges occur in the surface and above the bottom boundary layer and reduce the under-ice shelf volume by 15% in 10 days. Under-ice along-shore pressure gradients established by along- and cross-shore variations in ice width and/or under-ice friction alter this basic circulation pattern. For a landfast ice zone of finite width and length, upwelling-favorable winds blowing seaward of and transverse to the ice boundaries induce downwind flow beneath the ice and generate vorticity waves that propagate along-shore in the Kelvin wave direction. Our results imply that landfast ice dynamics, not included explicitly herein, can effectively convert the long-wavelength forcing of the wind into shorter-scale ocean motions beneath the landfast ice.

Citation: Kasper, J. L., and T. J. Weingartner (2012), Modeling winter circulation under landfast ice: The interaction of winds with landfast ice, *J. Geophys. Res.*, *117*, C04006, doi:10.1029/2011JC007649.

1. Introduction

[2] Winds and river runoff influence the dynamics and circulation over continental shelves, particularly the inner shelf (depths < ~20 m). While true for Arctic shelves as well, the effects of wind stress and buoyancy are substantially modulated by the annual freeze/thaw cycle, which controls the phasing and duration of the landfast ice season and river discharge [*Weingartner et al.*, 2009]. Landfast ice, which covers the inner shelf from ~October through June, is essentially immobile and thus inhibits momentum transfer from the wind to the ocean. This ice also exerts a frictional stress on the under-ice flow, hence, the circulation dynamics within the landfast ice zones surrounding the Arctic Ocean are quite different than those of ice-free shelves.

[3] In the Alaskan Beaufort Sea (ABS), the circulation seaward of the landfast ice zone is vigorous (~0.2–1 m s^{-1}) and wind-forced [e.g., *Aagaard and Roach*, 1990; *Pickart et al.*, 2009], whereas beneath the landfast ice cover, currents are small ($\leq$0.05 m s^{-1}) and uncorrelated with local or regional winds [*Weingartner et al.*, 2009]. Prevailing winds over the ABS are northeasterly year-round and on average promote upwelling. The along-shelf wind stress varies seasonally with upwelling winds maximum in late fall and minimum in summer [*Weingartner et al.*, 2009]. The synoptic variability is large and dictated by the passage of storms generated in both the Arctic and Pacific oceans [*Pickart et al.*, 2009]. The former are most prevalent in late-summer and early fall and result in downwelling, and the latter are common throughout the late-fall and winter (during the landfast ice season) and lead to upwelling [e.g., *Pickart et al.*, 2009]. Within the landfast ice zone the flow is controlled by along- and cross-shore pressure gradients (of uncertain origin) and frictional coupling with the underside of the ice and seabed.

[4] Friction between landfast ice and the ocean is poorly understood, but will depend on both the under-ice topography and current speed [e.g., *Lu et al.*, 2011]. Under-ice topography on windward shelves, such as the ABS, is rough due to collisions at the seaward boundary with the wind-driven pack ice. Ridging intensity and keel depths generally increase offshore and throughout the freezing season, although these features can vary substantially in the along-shore direction [*Tucker et al.*, 1979]. In addition, the landfast ice width varies along the ABS [*Mahoney et al.*, 2007]. These

[1]Institute of Marine Science, University of Alaska Fairbanks, Fairbanks, Alaska, USA.
[2]Now at Department of Physical Oceanography, Woods Hole Oceanographic Institution, Woods Hole, Massachusetts, USA.

0148-0227/12/2011JC007649

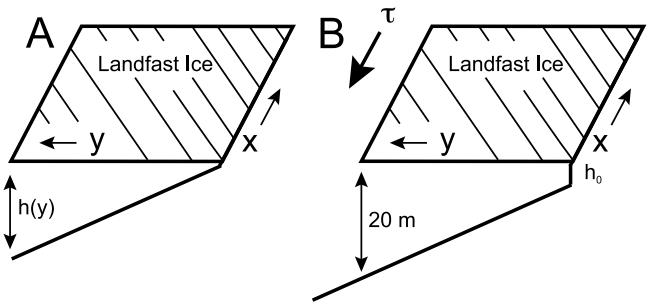

Figure 1. (a) The coordinate system for the analytic model, with the coast along y = 0 and depth increasing linearly with distance offshore, $h = sy$. (b) The numerical model domain where $h = h_0 + sy$ (h_0 is the depth of the coastal wall). The bottom slope, $s = 7.5 \times 10^{-4}$, is identical in both the analytical and numerical models and it is comparable to the Alaskan Beaufort Sea shelf bottom slope. Whereas the analytical domain encompasses just the area under the landfast ice, the numerical domain includes the area offshore of the ice edge where a spatially uniform upwelling (0.1 N m^{-2} ~ 7 m s^{-1}) wind blows parallel to the coast.

considerations suggest that ice-water friction will also vary over a range of time and spatial scales and complicate the circulation response.

[5] *Shirasawa* [1986] measured ice-ocean drag beneath landfast ice in the Canadian Archipelago and found that the quadratic under-ice drag coefficient ranged from 5×10^{-3} for smooth ice to 9×10^{-3} for rough ice. *McPhee* [1990] found a similar range for pack ice. They also noted that the drag coefficient varied substantially over short distances, and attributed the variations to form (pressure) drag associated with deep ice keels. Their results suggest that the range in values for a linear ice-ocean friction coefficient (r_{ice}) is between 10^{-4} and 10^{-3} m s^{-1}.

[6] J. L. Kasper and T. J. Weingartner (The effect of landfast ice on a lateral inflow to a shelf sea, submitted to *Continental Shelf Research*, 2010, hereinafter referred to as KW) used a vertically averaged, linear, steady state vorticity equation that mimics the effects of landfast ice by imposing a surface stress (no-slip condition) on the ocean surface. The stress is assumed to be related to the under-ice velocity through r_{ice}, a linear friction coefficient, which could vary in both the along- and cross-shore directions. Their vorticity equation, termed the arrested landfast ice topographic wave equation (ALW), mimics *Csanady*'s [1978] arrested topographic wave (ATW) model. KW used the ALW vorticity equation to examine the effect of landfast ice on an along-shore geostrophic inflow imposed at one end of a shelf domain covered by landfast ice of finite width. KW found that because of the frictional coupling between the ice and the ocean (and between the bottom and the ocean) the effect of constant upstream (in the Kelvin wave sense) cross-shelf sea level slope was rapidly attenuated ~50 km downstream of the imposed sea level slope. Thus we expect local mechanisms (local winds) and/or propagating signals (e.g., shelf waves) interacting with the ice cover to be of primary importance to currents under landfast ice, far removed from elevated (or depressed) sea levels.

[7] Here we use the ALW vorticity equation to examine the effect of a landfast ice cover on a cross-shore sea level slope that extends across the landfast ice zone and that is established by winds seaward of the ice edge. The simplified steady state ALW vorticity equation is used to set the stage and guide the discussion of the more complex, time dependant numerical results. The simplified ALW vorticity equation retains enough complexity to illustrate the relation between the under-ice sea level response, upwelling favorable winds and under-ice friction while still allowing for the insight provided by an analytical solution. While ice edge processes have been considered before, previous studies [e.g., *Gammelsrod et al.*, 1975; *Clarke*, 1978; *Fennel and Johannessen*, 1998] concentrated on wind-forced motions near the ice edge rather than the circulation beneath the ice. In addition, they assumed a constant bottom depth, that the ice edge was far from any coastal boundaries, and they ignored along- and cross-shore variations in ice properties, including under-ice friction. Initially, we describe, in detail, the response of nearshore circulation beneath a uniform immobile landfast ice cover to winds seaward of the ice edge. Model experiments are designed to understand and suggest reasons for the observed breakdown of the wind-current relationship under landfast ice [e.g., *Weingartner et al.*, 2009] and we end the paper with an examination of how spatial variations in ice extent and in under-ice friction affect this response. Because of the prevalence of upwelling winds in the ABS associated with synoptic storms of limited duration, numerical experiments focus solely on the under-ice subtidal response to upwelling winds at short time periods (<10 days). The paper proceeds as follows. Section 2 describes the simplified (ALW) vorticity equation. Numerical experiments examining the flow under landfast ice subject to upwelling favorable winds offshore of the landfast ice edge are described in section 3. Section 4 discusses relevant observations and summarizes the paper.

2. A Simplified Vorticity Equation

[8] To demonstrate the first order effect of landfast ice on inner shelf circulation an analytic description of steady barotropic subtidal flow beneath landfast ice was developed based on the ATW vorticity equation, which considers the effects of a sloping, frictional bottom on a steady coastal flow. For the ALW, we modify the steady state, vertically averaged, long wave, ATW governing equations to include landfast ice as a surface stress. This stress is analogous to placing a bottom boundary layer on the ocean surface. A simple solution to the ALW vorticity equation illustrates the effect of under-ice friction on the sea level anomaly beneath the ice.

[9] Our model domain is a rectangle bounded by a straight coastline along the southern boundary ($y = 0$, with x the along-shore coordinate; Figure 1a). The northern boundary is the landfast ice edge ($y = L$, with L the width of the landfast ice). Figure 1b is the numerical model domain, which encompasses the entire shelf (the inner shelf under the landfast ice and the area offshore of the ice edge). We assume that bottom depth, h, increases linearly with distance offshore: $h = sy$, $s = 7.5 \times 10^{-4}$, the approximate slope of the ABS [e.g., *Danielson and Johnson*, 2008]. Bottom and

under-ice friction are linearly related to the depth averaged under-ice transport. From Appendix A, the governing equations are:

$$\left.\begin{aligned} fv &= -g\frac{\partial\eta}{\partial x} + \frac{-(r_{ice}+r_b)u}{h} + F_x && \text{along-shore momentum}\\ -fu &= -g\frac{\partial\eta}{\partial y} + \frac{-(r_{ice}+r_b)v}{h} && \text{cross-shore momentum}\\ \frac{\partial(uh)}{\partial x} &+ \frac{\partial(vh)}{\partial y} = 0 && \text{continuity} \end{aligned}\right\} \quad (1)$$

F_x is the wind stress in the along-shore direction (zero everywhere under the ice). The cross-shore velocity, v, is positive to the north, the along-shore velocity, u, is positive to the east, η is the sea level anomaly, r_b is the constant bottom friction coefficient, f is the Coriolis parameter (taken as $f = 1.37 \times 10^{-4}$ m s^{-1} for $\varphi = 70°$N), h ($= sy$) is the bottom depth and r_{ice} is the under-ice friction coefficient. Note the signs of the bottom and under-ice frictional stresses ($-(r_{ice}+r_b)u/h$, $-(r_{ice}+r_b)v/h$) are the same.

[10] Following *Csanady* [1978] we assume the cross-shore stress, $(r_{ice}+r_b)v/h$, is small compared to the along-shore stress so that the cross-shore momentum balance is geostrophic: $fu = -g\partial\eta/\partial y$. Beneath the ice, the along-shore wind stress curl is zero (the ice edge boundary condition represents the effect of the wind stress curl at the ice edge). Taking the curl of the governing equations and neglecting the wind stress curl leads to the vorticity equation for the area under the landfast ice cover:

$$\underbrace{\frac{\partial\eta}{\partial x}}_{\substack{\text{Vortex}\\ \text{Stretching}}} = \underbrace{\frac{(r_{ice}+r_b)}{fs}\frac{\partial^2\eta}{\partial y^2}}_{\substack{\text{Term 1}\\ \text{Divergence by}\\ \text{Frictional Stresses}}} + \underbrace{\frac{1}{fs}\frac{\partial(r_{ice}+r_b)}{\partial y}\frac{\partial\eta}{\partial y}}_{\substack{\text{Term 2}\\ \text{Frictional Curl}}}. \quad (2)$$

Equation (2) is the ALW or under-ice vorticity equation and is derived in the appendix. It describes the effects of bottom friction, rotation, a sloping bottom and spatial variability in the ice-ocean friction on the sea level anomaly beneath a landfast ice cover. The ALW vorticity shows how spatial variations in the ice-ocean friction results in divergence in the geostrophic transport. This gives rise to vortex stretching, in terms of the along-shore sea level slope, $\partial\eta/\partial x$.

[11] The ALW model is a parabolic advective-diffusive, differential equation, where the diffusion coefficient, $\kappa = (r_{ice}+r_b)/fs$ may vary with position. *Csanady*'s [1978] ATW model is a diffusion equation,

$$\frac{\partial\eta}{\partial x} = \frac{r_b}{fs}\frac{\partial^2\eta}{\partial y^2},$$

with a constant diffusion coefficient, $\kappa = r_b/fs$. Term 1 of the ALW vorticity equation is diffusive-like and describes vorticity changes due to the joint effects of a sloping bottom, rotation and under-ice and bottom friction. As in the ATW, diffusion is proportional to the cross-shore gradient of the along-shore geostrophic velocity, i.e., term 1 is related to the relative vorticity. Term 2, the advective-like term, is the cross-shore gradient in ice friction multiplied by the along-shore geostrophic transport, i.e., the curl of the along-shore friction. The sign of $\partial(r_{ice}+r_b)/fs\ \partial y$ is assumed positive in our setting since landfast ice roughness in the ABS generally increases with offshore distance [*Tucker et al.*, 1979], which we mimic by increasing r_{ice} with distance offshore. This term implies that spatial variations in ice-ocean friction induce frictional torques on the water column.

[12] In midlatitude studies of wind-driven shelf circulation, the wind stress is often applied over the length of the shelf [e.g., *Gill and Schumann*, 1974] and enters into the coastal boundary condition. In the ice-free case, steady state develops at the coast shortly after the onset of wind-forcing (in shallow water) and propagates offshore with increasing time (toward deeper water). Since ice covers our domain, forcing must be applied elsewhere; KW considered a geostrophic inflow along the western boundary, upstream (in the Kelvin wave sense) of the domain. Here we specify the forcing by prescribing the sea level at the offshore landfast ice edge, i.e., the northern boundary of the analytical model domain. Note, for the steady state analytical solution we specify a finite sea level anomaly to represent the effect of the infinite wind stress curl at the edge of the landfast ice rather than specify the infinite windstress curl as an analytically difficult delta function. Instead we use the numerical results to study the effects of an infinite surface stress curl at the ice edge on under-ice circulation. While the analytical solution does not depend on time, in the time dependant numerical results, the forcing signal propagates shoreward from the ice edge (opposite the ice free case).

[13] The coastal boundary condition is no flux through the coast, i.e., $vh = 0$ at $y = 0$. When combined with the along-shore momentum equation in equation (1), the coastal constraint implies that $\partial\eta/\partial y = 0$ at $y = 0$ (where we have set $h = 0$ at $y = 0$ and used the cross-shore momentum balance to set $u = -(g/f)\,\partial\eta/\partial y$).

[14] In the absence of along-shore variations in ice or winds ($\partial\eta/\partial x = 0$) and a constant sea level at the ice edge ($\eta = \eta_0$ at $y = L$), a simple solution to the ALW vorticity equation (equation (2)) is easily found. In this case, equation (2) reduces to:

$$\frac{\partial}{\partial y}\left[\frac{(r_{ice}+r_b)}{fs}\frac{\partial\eta}{\partial y}\right] = 0 \quad (3)$$

To proceed, we assume that the friction coefficient varies in the cross-shelf direction as $(r_{ice}+r_b) = C_1(C_2+C_3y)^2$, a parameterization that mimics the presumed offshore increase in ice roughness. Integration of equation (3) yields:

$$\eta = \frac{-fsC}{C_1C_3(C_2+C_3y)} + c \quad (4)$$

where C and c are integration constants. Application of the coastal constraint implies that $C = 0$ so that $\eta = \eta_0$ everywhere beneath the ice cover. Hence, in the absence of along-shore changes in ice or winds, the ALW vorticity equation predicts that nearshore currents beneath landfast ice (driven by a surface stress curl across the ice edge) eventually decay to zero. Note that in the case of constant r_{ice}, the ALW vorticity equation reduces to the ATW vorticity equation. In this simple scenario the solution is identical for both vorticity equations; no flow under the ice. *Gammelsrod et al.* [1975]

Table 1. Range of Ice Parameters Considered[a]

	C_1	C_2	C_3	$m = 2\pi/M$, M (km)	Ice Width, L (km)
Base (analytic)	2×10^{-2}	10^{-1}	10^{-6}	NA	25
Numerical	10^{-3}–10^{-1}	10^{-3}–10^{-1}	10^{-5}–0	M = 200–1200	10–75

[a]Range of r_{ice} considered: 0–10^{-3} m s^{-1}.

obtained this result for a flat-bottomed, marginal ice zone setting of infinite extent and no coastal wall. Consistent with *Gammelsrod et al.*'s [1975] analytical solution, numerical results show that the steady state is approached because of offshore under-ice transport in the surface and bottom boundary layers.

[15] While this solution to the ALW vorticity equation is particularly simple, numerical results show how the under-ice currents evolve through time and that the cross-shore sea level slope ($\partial\eta/\partial y$)and under-ice sea level (η) depend upon the magnitude and cross-shore variation in the friction coefficient, r_{ice}. This dependence follows from equations (3) and (4).

3. Numerical Model Results

3.1. Model Description

[16] The process model experiments were conducted with the Regional Ocean Modeling System (ROMS) [*Shchepetkin and McWilliams*, 2005; *Song and Wright*, 1998] that solves the primitive equations. ROMS is a finite difference, free surface model with stretched, terrain-following coordinates in the vertical (s-coordinate [*Song and Haidvogel*, 1994]). The s-coordinate is desirable when dealing with continental shelf topography and allows for increased resolution in the top and bottom boundary layers. The time stepping scheme is split between the fast (vertically averaged) and slow (baroclinic) modes. Sensitivity studies (to ice parameters) were conducted with ROMS configured to solve just the vertically averaged (2-D) mode. ROMS variables are defined on a staggered "Arakawa C" grid [*Arakawa and Lamb*, 1977].

[17] We also configured ROMS to solve the full set of coupled primitive equations for an unstratified water column beneath a landfast ice cover. For the three-dimensional (3-D) experiments, we use the Mellor-Yamada level 2.5 [*Mellor and Yamada*, 1982] mixing scheme, where eddy diffusivity depends upon the local flow and stratification. We used 40 s-levels with the vertical levels stretched for high resolution in the surface and the bottom boundary layers.

[18] Tests showed that $\Delta\eta/\Delta y$ was insensitive to a 0.5 or 1 km horizontal resolution, but that a 0.5 km resolution was better for studying the complex circulation near the ice edge in the 3-D experiments. Therefore we used a resolution of 500 m and 1 km in the cross- and along-shore directions, respectively, in the 3-D experiments and a uniform 1 km grid in the 2-D experiments. The nonlinear terms are retained in both the 2-D and 3-D experiments.

[19] As with the ALW vorticity equation, landfast ice, of constant thickness, enters the model experiments only through a surface stress that is linearly related to the under-ice velocity. In the 3-D experiments, the surface stress, $\tau_{surf} = -\rho_0 r_{ice}\vec{u}_{surf}$, where $\vec{u}_{surf}$ is the surface velocity and r_{ice} has units of m s^{-1}. In the vertically averaged numerical experiments surface stress is linearly related to the depth-averaged under-ice transport. Landfast ice extent is prescribed by choosing the spatial extent of r_{ice} and by applying a spatially uniform upwelling favorable wind stress (an easterly, 0.1 N m^{-2} wind stress of $\sim$7 m s^{-1} ramped up over two days) everywhere $r_{ice} = 0$ m s^{-1}.

[20] Figure 1b shows the numerical model setting. The bathymetry mimics the ABS and the bottom depths and slope are the same as in the analytical ALW solution (with $h_0 = 0.1$ m in the numerical model). The ROMS "WET_DRY" option is employed to allow the sea level to drop below the coastal wall depth. The model domain is a 600 km long shelf, oriented east-west ($0 < x < 600$ km), with the coastal wall along the southern boundary. The along-shore boundaries are periodic and no gradient conditions apply on all variables at the northern (or offshore) boundary. The cross-shore extent of the domain is 200 km (with the coast at $y = 0$ and $0 < y < 200$ km). There are no along-shore variations in the bathymetry or the coastline.

[21] We also set $r_{ice} = C_1(C_2 + C_3 y)^2$ (in contrast to the ALW vorticity equation, here the surface and bottom stresses are now specified separately with $r_b = 10^{-4}$ m s^{-1}). The range of values for C_1, C_2, C_3, and ice width considered is listed in Table 1 and the r_{ice} for different cases are shown in Figure 2. We call the 2-D case with $C_1 = 10^{-2}$, $C_2 = 10^{-1}$ and $C_3 = 10^{-6}$ the basic ALW-like numerical simulation. We compare the variable r_{ice} experiments with simulations in which r_{ice} does not vary across the shelf. We call the case where $r_{ice} = 10^{-4}$ m s^{-1} the basic ATW-like numerical simulation. In the basic ALW-like numerical simulation, we examine small cross-shore variations in r_{ice} such that $r_{ice} \sim r_b$.

[22] For most experiments, the ice edge parallels the coast (with landfast ice covering the area inshore of the 20 m isobath, so that in the basic 2-D case, wind stress is applied

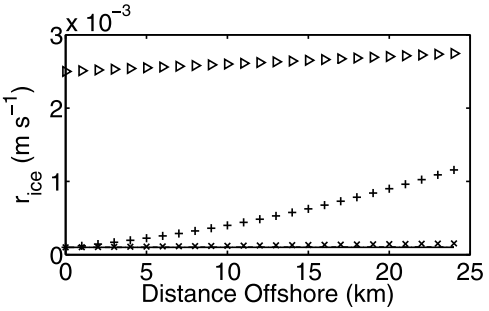

Figure 2. The ice-ocean friction coefficient, $r_{ice} = C_1(C_2 + C_3 y)^2$. Crosses mark the basic case ($C_1 = 10^{-2}$, $C_2 = 10^{-1}$, $C_3 = 10^{-6}$). Plus signs are for $C_1 = 10^{-2}$, $C_2 = 10^{-1}$, $C_3 = 10^{-5}$. Triangles mark the case with $C_1 = 10^{-2}$, $C_2 = 5 \times 10^{-1}$, $C_3 = 10^{-6}$. The solid line is the constant r_{ice} coefficient ($r_{ice} = 10^{-4}$ m s^{-1}). The range of r_{ice} of 10^{-4} and 10^{-3} m s^{-1} was investigated using numerical simulations.

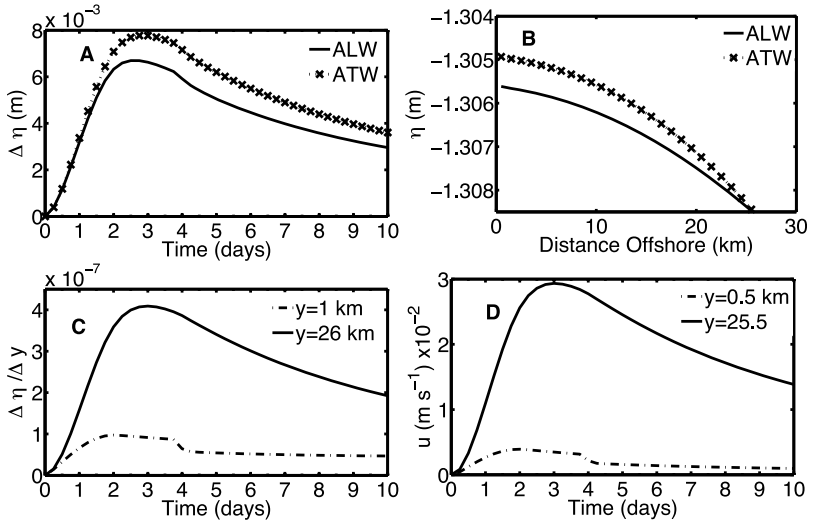

Figure 3. (a) Sea level difference between the coast and the ice edge for the basic ALW- and ATW-like simulations versus time. (b) The sea level anomaly between the coast and the ice edge after 10 days for the basic ALW- and ATW-like simulations. (c) The cross-shore sea level slope near the coast (y = 1 km) and near the ice edge (y = 26 km) versus time from the basic ALW-like simulation. (d) The along-shore velocity, u, near the coast and the ice edge from the basic ALW-like simulation. Note that the y-location of $\Delta\eta/\Delta y$ and u differ because of the staggered grid.

seaward of $y \geq 26.5$ km). Other experiments consider various ice widths. We define the location of the ice edge to be one grid point shoreward of the first grid point over which the wind stress acts In the basic 2-D this is at y = 25.5 km.

3.2. The Basic Vertically Averaged Experiments

[23] The basic ALW- and ATW-like results of Figure 3 are similar to previous studies of ice edge upwelling [e.g., *Gammelsrod et al.*, 1975]. Sea surface height is a minimum at the edge of the landfast ice zone, under westward winds and no along-shore variations in r_{ice}, due to the surface stress curl at the ice edge. Here the sea level decreases nearly linearly with time so that by day 10 sea level has dropped by ~ -1.3 m. Sea level increases with offshore distance from the ice edge, which results in a westward-flowing (downwind) ice edge current jet of ~ -1 m s^{-1} after 10 days. Note that in the basic cases $\Delta\eta/\Delta x = 0$ because there are no along-shore variations in ice parameters.

[24] In comparing the basic ALW- and ATW-like models we present the sea level differences ($\Delta\eta$) between the coast and the ice edge (Figure 3a) and sea level anomaly (η) as a function of distance from the coast (Figure 3b) after 10 days for the region under the landfast ice only. For the basic ALW-like simulation we show $\Delta\eta/\Delta y$ at both the coast and at the ice edge (Figure 3c) and the along-shore velocity (u; Figure 3d) at the coast and the ice edge. All variables are plotted as a function of time, t.

[25] Figures 3a–3d suggest that the basic adjustment proceeds as follows. At t = 0 upwelling favorable winds initiate a decrease in sea level at the ice edge and the developing cross-shore sea level slope between the coast and the ice edge drives an upwind (eastward), under-ice geostrophic current. The ice and seabed induce frictional stresses on the along-shore flow that impel cross-shore transport toward the ice edge.

[26] Hence, adjustment propagates inshore from the ice edge. From Figure 3c, the maximum magnitude of $\Delta\eta/\Delta y$ (e.g., $|\Delta\eta/\Delta y|$) occurs at 2.5 days for the ALW-like model (2.75 days for the ATW-like model) when the forcing signal reaches the coast. Thereafter, $|\Delta\eta/\Delta y|$ diminishes because the coastal sea level decreases more rapidly than the ice edge sea level. We define the frictional adjustment time, t_f, as the time between t = 0 and when $|\Delta\eta/\Delta y|$ attains its maximum.

[27] Figures 3a and 3c show that $\Delta\eta/\Delta y$ depends upon the form of r_{ice} and that sea level differences (Figure 3b) are largest at the coast. For constant r_{ice} (the ATW-like model) the coastal sea level is O(10^{-3} m) higher than for the variable r_{ice} (the ALW-like model), although the ice edge sea level is identical in both cases.

[28] Figure 3c shows that throughout the 10-day run, $|\Delta\eta/\Delta y|$ is a minimum at the coast and maximum at the ice edge. The time evolution of the along-shore upstream geostrophic velocity (Figure 3d) reflects the time and spatial variation of $\Delta\eta/\Delta y$. Initially the along-shore under-ice velocity increases everywhere (but most rapidly near the ice edge). For $t > t_f$, the along-shore under-ice velocity decreases. The smallest along-shore velocities (<0.01 m s^{-1}) are at the coast, and the largest velocities (maximum $\sim$ 0.03 m s^{-1}) are at the ice edge. By day 10, $\Delta\eta/\Delta y$ between the coast and the ice edge is -1.1×10^{-7}, and supports a mean along-shore geostrophic velocity of 0.008 m s^{-1}. The linear and nonlinear solutions are very similar although the nonlinear solution yields slightly greater offshore under-ice transport, which results in sea level being about 1 mm lower after 10 days than for the comparable linear experiment.

3.3. Three-Dimensional Results

[29] The 3-D results allow an examination of the under-ice velocity structure (Figures 4–7). Figure 4a and 4b are the along-shore and cross-shore velocities between the coast and

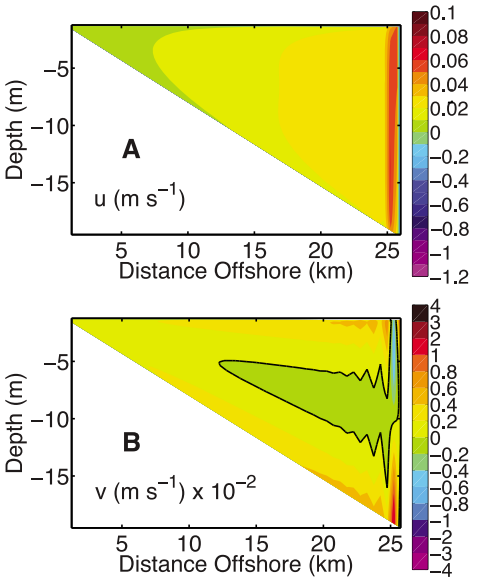

Figure 4. The cross-shelf distribution after 10 days of (a) along-shore velocity (m s^{-1}) inshore of the ice edge (positive velocities imply flow out of the page). The positive contour interval is 0.01 m s^{-1}. The negative contour interval is 0.1 m s^{-1}. (b) Cross-shore velocity (m s^{-1}, positive velocities indicate offshore flow). The solid black contour indicates the zero contour.

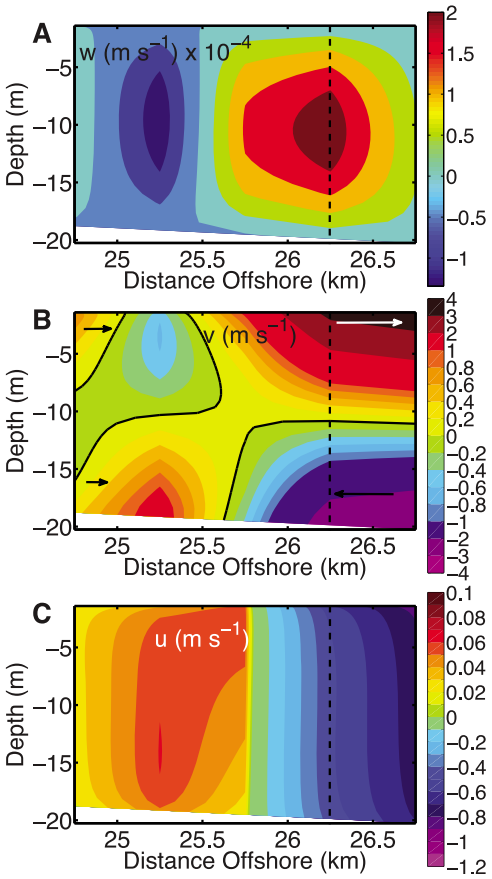

Figure 6. The cross-shelf distribution in the vicinity of the ice edge after 10 days for the basic 3-D experiment of the (a) vertical velocity, *w*, (positive velocities are up), (b) cross-shore velocity, *v*, and (c) along-shore velocity, *u*. B, the solid black line, is the zero contour. In Figure 6c the positive contour interval is 0.01 m s^{-1}, whereas for negative velocities the contour interval is 0.1 m s^{-1}. The vertical line indicates the grid point where the wind stress is applied (26.25 km from the coast). Arrows schematically represent the direction of flow in Figure 6b and are not to scale.

y = 25.75 km 10 days after the onset of the wind. In Figures 4a and 4b the ice edge is at y = 25.75 km and winds are applied at, and seaward of, y = 26.25 km. The along-shore, under-ice flow is eastward (upwind) and largely geostrophic with velocities diminishing from ~ 0.06 m s^{-1} near the ice edge to less than 0.01 m s^{-1} within 10 km of the coast. Under-ice cross-shore velocities (Figure 4b) are offshore within the surface and bottom boundary layers and near the ice edge, but weakly onshore at mid-depths. Note the presence of numerical noise in Figure 4b. Increasing the resolution (vertical and horizontal) did not modify the qualitative appearance of the noise (the scale remained on the order of the grid spacing). As noted above, quantitatively, the cross-shore transport does not depend on the resolution. Further, the magnitude of the noise remains on the order of the ambient flow as the flow field evolves with time. The convergent flow visible in the upper right corner of Figure 4b is part of a complex circulation cell near the ice edge that is discussed below. Overall, because of the presence of convergent flow at the surface, slightly shoreward of the ice edge, and offshore flow in the bottom boundary layer,

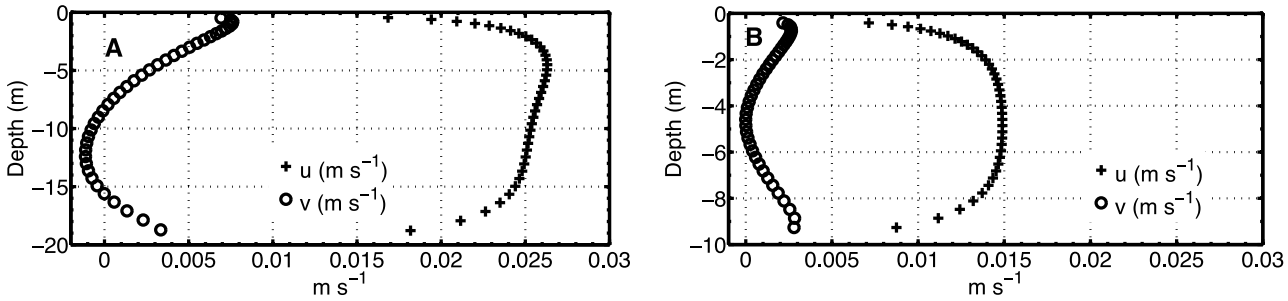

Figure 5. Vertical profiles of the horizontal velocity components (m s^{-1}) beneath the landfast ice cover after 10 days of upwelling-favorable wind stress over (a) the 19 m isobath and (b) the 10 m isobath. Note that the y-axis scales differ between Figures 5a and 5b.

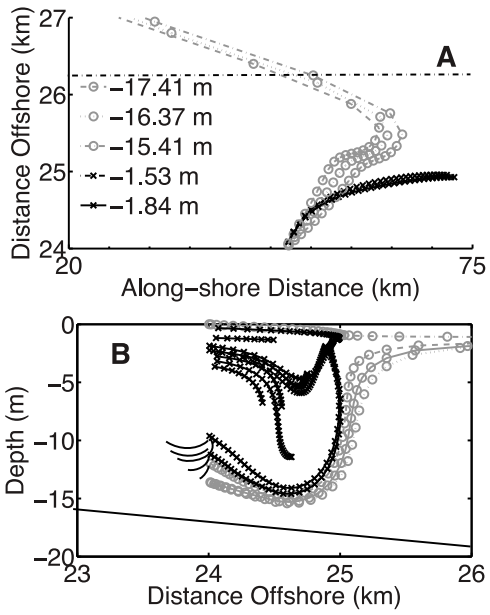

Figure 7. Particle trajectories in (a) the *x*-*y* plane and (b) the *y*-*z* plane. In Figure 7a, particles that cross the ice edge are denoted by gray lines with circles and those that remain inshore of the ice edge are indicated by black lines with crosses. In Figure 7a the ice edge is marked by the horizontal line at $y = 26.25$ km, the release depth of the particles is indicated in the legend, and markers are spaced 0.25 days apart. In Figure 7b, particles are initialized at 24 km offshore. Trajectories marked by gray circles cross the ice edge, trajectories marked by black crosses move offshore though remainshoreward of the ice edge during 10 days considered. Solid black lines without markers indicate particles that move shoreward. The bottom is indicated by the sloping solid line.

Figure 4b suggests that the water that escapes from under the ice is derived mainly from within and slightly above the bottom boundary layer. Particle trajectories discussed below confirm this.

[30] Figure 5a shows vertical profiles of the along-(u) and cross-shore (v) velocities at the 19 m isobath (24.75 km from the coast and 1 km inshore of the ice edge). The profiles in Figure 5b are from the 10 m isobath, midway between the ice edge and the coast. Surface and bottom friction result in a parabolic along-shore velocity profile with a mid-depth maximum similar to pipe flow [e.g., *Kundu and Cohen*, 2008]. However, the surface and bottom boundary layers are not symmetric because the seabed slopes whereas the surface boundary is essentially flat save for the slight tilt due to the sloping sea surface.

[31] The maximum in v is slightly below (above) the surface (bottom) boundary layer. Over the 19 m isobath, v is small and onshore between 7 and 15 m depth and offshore elsewhere. Nevertheless, the net cross-shore transport is positive indicating that offshore boundary layer transport is not balanced by onshore transport in the interior. Over the 10 m isobath (Figure 5b) the cross-shore velocities are positive everywhere. Hence the net cross-shore transport is offshore everywhere shoreward of the ice edge and causes the coastal sea level to decrease continuously over the 10-day period.

[32] Figures 6a–6c show the vertical velocity, w, and the v and u velocity components across the ice edge. Seaward of the landfast ice, v is offshore at $\sim$0.03 m s^{-1} in the surface boundary layer and onshore at similar speeds in the bottom boundary layer. Hence at the ice edge the bottom boundary layer cross-shore transports converge and feed upwelling shoreward of the ice edge (inshore to $\sim y = 25.5$ km). This results in a bottom to surface circulation cell visible in the w- and v-contours across the ice edge. Farther inshore, there is convergence in the surface boundary layer beneath the ice, which results in downwelling. The flow converges (diverges) where $\Delta\eta/\Delta y$ is negative (positive). Upwelling (downwelling) is maximum where the convergence (divergence) is greatest. Figure 6c shows that the along-shore velocity, u, is weakly upwind ($\sim$0.06 m s^{-1} maximum) inshore of the ice edge, but downwind at ~ -1 m s^{-1} seaward of the ice edge.

[33] Neutrally buoyant (dynamically passive) particles are used to illustrate the complexity of cross-shore transport under the landfast ice cover. Offshore particle displacement generally increases with offshore distance because both u and v increase seaward beneath the landfast ice. We will show trajectories for particles released more than 21 km offshore and state results for particles released shoreward of this point. First, no particles released within 21 km of the coast reached the ice edge during the 10-day period considered. Second, particles released 2 km from the coast and in the surface and bottom boundary layers move a maximum of 2 km offshore and 5 km eastward. Third, particles released in the surface and bottom boundary layer 12 (15) km from the coast move 2 (4) km offshore and 15 (20) km to the east and sink by $\sim$1 m in the surface boundary layer. Overall, particle trajectories support the hypothesis suggested by the cross-shore velocity contours (Figures 4b and 6b) that the water that escapes from under the ice is mainly derived from within and slightly above the bottom boundary layer.

[34] The largest displacements are for particles that cross the ice edge although their trajectory depends upon their release depth. Figure 7a shows a plan view of 10-day trajectories for particles released over the 19 m isobath between 12 and $\sim$17 m, at $y = 24$ km (or 1.75 km inshore of the ice edge). Initially, these particles move offshore, eastward, and upwards until they enter the ice edge jet, where they are then rapidly swept westward and offshore in the wind-driven surface layer. Overall, 75% of particles released 24 km offshore and at depths greater than 10 m transit across the ice edge.

[35] Figure 7b shows a subset of trajectories in the cross-shore plane for particles initialized at $y = 24$ km. Those particles that move offshore and across the ice edge are marked by circles and gray lines. After crossing the ice edge, these particles enter the ice edge jet and move into the page. These include particles released between 12 and 17 m as well as a small number released at the surface. Particles marked by crosses and in black lines move offshore but do not cross the ice edge during the 10-day run but instead move eastward (off the page). Among these are some particles released just below the surface that remain inshore of the ice edge and move $\sim$23 km to the east in 10 days. Initially these near surface particles sink $\sim$2 m and move offshore until they encounter the upwelling cell inshore of the ice edge. Thereafter they move eastward (and slowly rise). Other particles

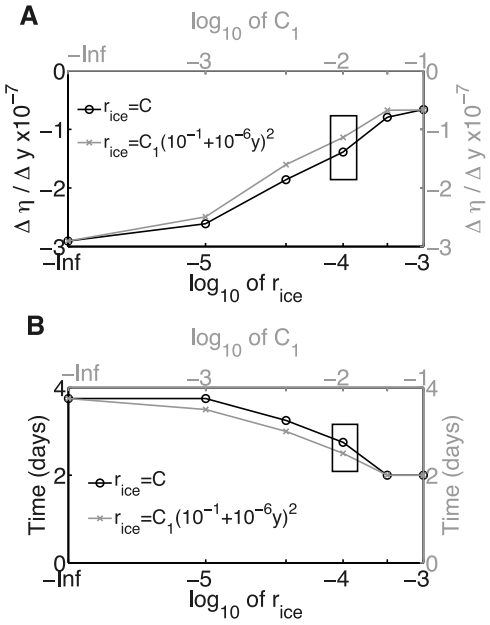

Figure 8. The cross-shore sea level slope and frictional adjustment time versus the magnitude of the ice-ocean friction coefficient. (a) The black circles denote the cross-shore sea level slope versus the $\log_{10}$ of the r_{ice} coefficient (for r_{ice} = constant). The gray crosses denote the cross-shore sea level slope versus the $\log_{10}$ of C_1 (for r_{ice} = variable) after 10 days. (b) The black circles denote the frictional adjustment time (t_f) versus the $\log_{10}$ of the r_{ice} coefficient (for r_{ice} = constant). The gray crosses denote t_f versus the $\log_{10}$ of C_1 (for r_{ice} = variable). The basic numerical ALW and ATW-like experiments are enclosed in the rectangles.

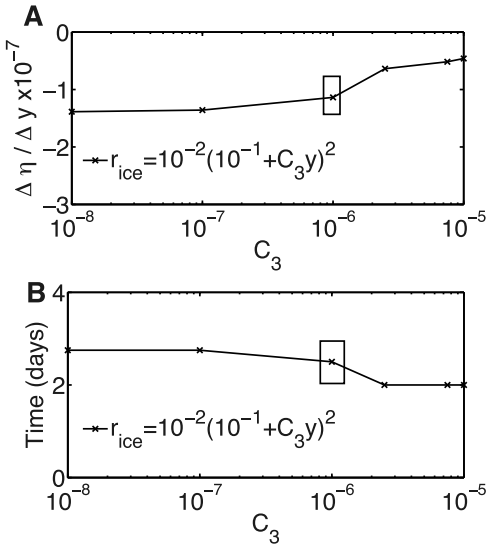

Figure 9. The (a) cross-shore sea level slope and (b) frictional adjustment time as functions of cross-shore variability in the ice-ocean friction coefficient. Results are shown after 10 days of model run. The basic numerical-ALW result is indicated by the rectangle.

(denoted by solid lines without markers) released further inshore between 10 and 15 depth at y = 24 km are carried inshore (and eastward) by the weak interior flow. In summary, our results suggest that exchange across the ice edge is limited to specific depths (at the surface and slightly above the bottom boundary layer) near the ice edge.

3.4. Sensitivity Analyses

[36] We now examine the sensitivity of the under-ice cross-shore sea level slope ($\Delta\eta/\Delta y$) to variations in r_{ice} (Figures 8 and 9) and ice width (Figure 10). The results are from vertically averaged model runs (without along shore variations) evaluated after 10 days of forcing by a 7 m s^{-1} upwelling favorable wind applied offshore of the ice edge. The plots show $\Delta\eta/\Delta y$ (estimated as the sea level difference between the coast and the ice edge divided by the ice width) and t_f, the time required to achieve the maximum slope.

[37] Figure 8a shows $\Delta\eta/\Delta y$ for the ATW-like model for constant r_{ice} (black circles) and for the ALW-like model (gray crosses) for $r_{ice} = C_1(10^{-1} + 10^{-6}y)^2$. For the ATW-like model runs the x-axis is the $\log_{10}(r_{ice})$, with $\log_{10}(r_{ice}) = -4$ being the basic ATW-like solution. For the ALW-like solutions the x-axis is the $\log_{10}(C_1)$ with $\log_{10}(C_1) = -2$ and $r_{ice} \sim 10^{-4}$ being the basic ALW-like numerical solution. Figure 8b shows t_f for both model types, with the x-axes as in Figure 8a. The basic ATW- and ALW-like numerical solutions are enclosed by boxes.

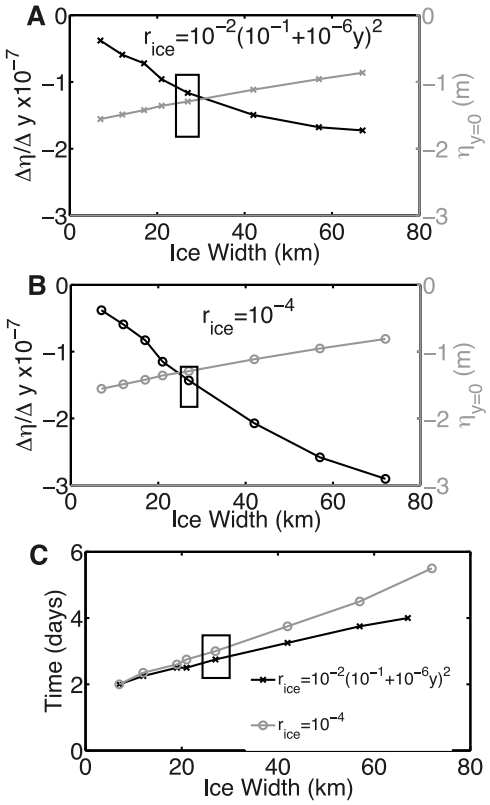

Figure 10. The cross-shore sea level slope versus ice width (black) and coastal sea level versus landfast ice width (gray) for (a) r_{ice} = variable and (b) r_{ice} = constant. The basic model with L = 25 km is indicated by boxed values. (c) The t_f versus ice width for r_{ice} = variable (black crosses) and r_{ice} = constant (gray circles).

[38] Figure 8 indicates that $\Delta\eta/\Delta y$ increases from $\sim -3 \times 10^{-7}$ to $\sim -10^{-7}$ and that t_f decreases from 4 to 2 days as r_{ice} increases from 0 to $\sim 10^{-3}$ ms^{-1}. In addition, $|\Delta\eta/\Delta y|$ and t_f are always slightly larger for the constant r_{ice} case compared to the variable r_{ice} case, although the magnitudes of both friction coefficients are similar. These differences are related to the vorticity balance discussed below. Variations in $|\Delta\eta/\Delta y|$ among experiments are mainly due to differences in the coastal sea level rather than sea level changes at the ice edge. As an example, for constant r_{ice} the coastal sea level depression is ~6 mm greater for $r_{ice} = 10^{-3}$ than for $r_{ice} = 0$, while the corresponding sea level difference at the ice edge is only ~0.2 mm. Net cross-shore transports are similar for all r_{ice} and differ by less than 1%. Over the 10 day model run, the cross-shore transport removes ~15% of the volume of the shelf inshore of the ice edge.

[39] We also examined the effect of changes in the magnitude of C_3 on $\Delta\eta/\Delta y$ (Figure 9a) and t_f (Figure 9b). (In Figures 9a and 9b both variables are plotted against the $\log_{10} C_3$ since $r_{ice} = 10^{-2}(10^{-1} + C_3 y)^2$, hence $\partial r_{ice}/\partial y$ varies with C_3.) The basic ALW-like numerical solution (with $C_3 = 10^{-6}$) is boxed. As C_3 increases from 10^{-8} to 10^{-5} ms^{-1}, $\Delta\eta/\Delta y$ increases from ~ -1.5 to $\sim -0.5 \times 10^{-7}$ and t_f decreases from ~2.5 days to 2 days. Differences in $\Delta\eta/\Delta y$ are again primarily due to differences in the coastal sea level drop but these vary by <0.5 mm over the range of C_3 examined. Net cross-shore transports at the ice edge are similar to the constant r_{ice} cases above and appear insensitive to the choice of C_3.

[40] Figures 10a–10c suggest how changes in landfast ice width affect the under-ice $\Delta\eta/\Delta y$ (black curves) and the coastal sea level (gray curves). In Figure 10a, $r_{ice} = 10^{-2}(10^{-1} + 10^{-6} y)^2$ while in Figure 10b, $r_{ice} = 10^{-4}$ m s^{-1}. Figure 10c shows t_f versus ice width, with black crosses for $r_{ice} = 10^{-2}(10^{-1} + 10^{-6} y)^2$ and gray circles for $r_{isce} = 10^{-4}$ m s^{-1}. In all cases, as ice width increases $|\Delta\eta/\Delta y|$ increases. For the constant r_{ice} case, $|\Delta\eta/\Delta y|$ increases with ice width but approaches a constant value for ice widths exceeding ~40 km when r_{ice} is variable.

[41] The variations in $\Delta\eta/\Delta y$ and coastal sea level with ice width over a sloping bottom are primarily a function of the time required to remove fluid from beneath the ice. As Figure 10c shows, t_f increases linearly with ice width from 2–4 days for variable r_{ice} and from 2–5.5 days for constant r_{ice}. This implies that more cross-shore transport and time is required to decrease coastal sea level by a set amount so that $|\Delta\eta/\Delta y|$ increases with increasing ice width.

3.5. The Vorticity Terms

[42] While $\Delta\eta/\Delta y$, coastal sea level and t_f concisely summarize the behavior of the solutions, the vorticity terms, which depend on the magnitude and distribution of r_{ice}, determine how these variables change with variations in ice parameters and how sea level and $\Delta\eta/\Delta y$ change with time. Moreover, while the simplified analytical vorticity equation, equation (2), is useful heuristically, the terms in that equation are not the only important vorticity tendencies; near the coast, numerical results indicate that the cross-shore stress terms neglected in the analytic model but retained in the numerical results (see the second of equation (1)) are ~2 orders of magnitude larger than the along-shore stress terms. The stresses near the coast and also at the ice edge contribute to the development of under-ice vorticity and thus the time variation of the relative vorticity cannot be ignored. In the absence of along-shore variations ($\partial/\partial x = 0$), the time dependent under-ice vorticity equation (equation (A4)) is

$$\underbrace{\frac{f}{sg}\frac{\partial \eta}{\partial t}}_{\text{Time variation in vortex stretching}} = \underbrace{\frac{(r_{ice}+r_b)}{sf}\frac{\partial^2 \eta}{\partial y^2}}_{\text{Term 1: Divergence by Frictional Stresses}} + \underbrace{\frac{1}{sf}\frac{\partial (r_{ice}+r_b)}{\partial y}\frac{\partial \eta}{\partial y}}_{\text{Term 2: Frictional Curl term}} - \underbrace{\frac{1}{sf}\frac{\partial}{\partial t}\left[\frac{\partial}{\partial y}\left(h\frac{\partial \eta}{\partial y}\right)\right]}_{\text{Term 3: Time variation of relative vorticity}} . \quad (5)$$

Equation (5) states that the local rate of change in vortex stretching (left hand side) is balanced by divergence due to frictional stresses (term 1), frictional curl (term 2), and the local rate of change in relative vorticity (term 3). Each term in equation (5) is negative. Terms 1 and 2 are sources of anticylonic vorticity, some of which increases anticyclonic relative vorticity (term 3) and some of which reduces sea level and so provides a squashing tendency.

[43] Figure 11 shows the cross-shore (y-axis) distribution through time (x-axis) of each term on the right-hand side of equation (5) for the basic ATW (r_{ice} = constant = 10^{-4} m s^{-1}) and basic ALW ($r_{ice} = r_{ice}(y) \sim 10^{-4}$ m s^{-1}) models where the ice edge is at y = 26.5 km. (Other choices of ice width show similar patterns and are not shown.) Terms 1 and 3 are common to both models, while term 2 is only in the ALW model. Figure 11a shows term 1 for the basic ATW solution whereas Figures 11b and 11c show terms 1 and 2 from the basic ALW solution.

[44] While the anticyclonic vorticity tendencies are reflected in the signs of the terms plotted in Figure 11, the following discussion is in terms of relative changes in the magnitude of each term. The magnitude of terms 1–3 increase rapidly for $t \leq \sim t_f$ and then decrease slowly afterwards. The magnitude of term 1 is only slightly larger in the ATW model than in the ALW model, but this term is 3–10 times greater than the magnitude of term 2 in the ALW model. The magnitude of term 2 is a minimum at the coast and a maximum at the ice edge. As C_3 (i.e., $\partial r_{ice}/\partial y$) increases, the magnitude of term 2 increases and the maximum magnitude of term 1 is shifted shoreward.

[45] Term 3 from the basic ALW model is shown in Figure 11d (its pattern is similar for the ATW model). It is largest near the ice edge where anticyclonic vorticity generation is greatest. (Note that near the coast there is a small increase in this term on day 3.75, just prior to the coastal boundary shifting one grid point offshore, as a consequence of the ROMS "WET_DRY" algorithm, and into deeper water. The peak corresponds to the maximum value of the cross-shore stress terms, which are inversely proportional to depth.) As the magnitude of r_{ice} or $\partial r_{ice}/\partial y$ increases, term 3 decreases slightly (by $\sim 1 \times 10^{-8}$ for the range of ice parameters considered) and its maximum develops sooner. For all r_{ice} = constant cases, the maximum value of term 3 is located at the ice edge, but as $\partial r_{ice}/\partial y$ increases, the maximum value shifts shoreward and the maximum develops sooner.

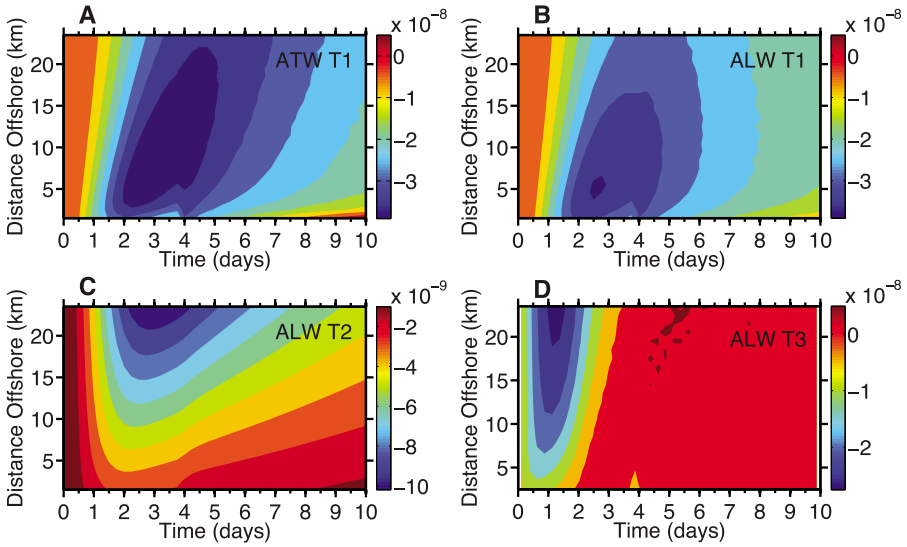

Figure 11. (a) The diffusive-like ATW vorticity term for $r_{ice} = 10^{-4}$ m s^{-1}. Figures 11b–11d are from the basic ALW-like numerical simulation and are the (b) relative vorticity or diffusive-like vorticity term (term 1), (c) frictional curl or advective-like vorticity term (term 2), and (d) the time rate of change of the relative vorticity (term 3). Terms 1–3 refer to the expressions in equation (5).

[46] The difference between term 3 and the sum of terms 1 and 2 gives rise to vortex squashing, which has very little cross-shore variation and hence is not shown. Squashing increases rapidly for $t < t_f$ to a maximum $\sim 4 \times 10^{-8}$ and then decreases slowly thereafter.

3.6. Along-Shore Variations in Under-Ice Friction

[47] We next consider how along-shore differences in r_{ice} affect along-shore sea level slopes within the landfast ice zone. We examine the response to a spatially uniform, 7 m s^{-1} upwelling favorable wind offshore of the landfast ice for the case where r_{ice} varies along the shelf according to: $r_{ice} = [C_0 + C_1 \sin(mx)]10^{-2}$. (We also conducted experiments in which $r_{ice} = [C_0 + C_1 \sin(mx)](C_2 + C_3 y)^2$ but these results are similar and not presented.) The results are shown in Figure 12, with Figures 12a–12d based on $m = \pi/75$ km^{-1} and Figures 12e–12h based on $m = \pi/150$ km^{-1}. In both cases, $0 < r_{ice} < O(10^{-4}$ m s$^{-1})$. The sea level patterns resemble "shelf circulation cells" associated with a spatially periodic windstress along a coast [*Csanady*, 1981], with the cell size dependent on m.

[48] The pattern develops due to along-shore differences in transport associated with along-shore variations in r_{ice}. This results in an additional vorticity tendency in the vertically averaged, steady state under-ice vorticity balance (equation (A5)) in which $r_{ice} = r_{ice}(x)$:

$$\frac{\partial \eta}{\partial x} = \frac{1}{gs}\left[(r_b v)_x - (r_b u)_y + (r_{ice} v)_x - (r_{ice} u)_y\right] \qquad (6)$$

where the x, y subscripts denote partial differentiation. The numerical results show that near the ice edge, and slightly up- and downstream of where $\partial r_{ice}/\partial x$ is maximum, all the stress terms are $O(10^{-7})$ and $\partial\eta/\partial x$ varies between $\pm 6 \times 10^{-8}$.

[49] At the coast, the along-shore velocity varies inversely with m; the minimum u is ~ -0.03 m s^{-1} for $m = \pi/75$ km^{-1} and the minimum u is ~ -0.06 m s^{-1} for $m = \pi/150$ km^{-1}. Additional experiments suggest that if the wavelength of the along-shore under-ice variations is $< \sim 32$ km (the barotropic Rossby radius in 2 m of water), then u near the coast is of the same order of magnitude as experiments with no along-shore variations in r_{ice}. The net cross-shelf transport after 10 days amounts to $\sim$14% of the total under-ice volume and differences in cross-shelf transport between the two cases is only $\sim$1%.

[50] There is also a time-varying response to steady winds when r_{ice} varies along-shore. However, the amplitude of the time-dependent along-shore sea level slope is two orders of magnitude less than the steady along-shore sea level slope. This response has a period of $\sim$3.5 days and persists throughout the 10-day run.

3.7. Along-Shore Variations in Ice Width

[51] Although along-shore variations in the magnitude of r_{ice} are unknown, along-shore variations in ice width occur on the Alaskan Beaufort shelf [*Mahoney et al.*, 2007]. Modeling along-shore changes in ice width proved difficult because of numerical noise generated at the ice edge. An example of the sea level anomaly, η (m), and vertically averaged along-shore velocity, u (m s^{-1}) from a linearized experiment, in which ice width varies sinusoidally from a minimum of 30 km to a maximum of 70 km between 0 and 600 km along the coast, is shown in Figure 13. The results suggest that sea level and along-shore current fields associated with variations in landfast ice width may be quite complex. For example, the flow at the ice edge is jet-like and westward everywhere but convergent over the westernmost 200 km and divergent over the easternmost 200 km. In contrast, while the under-ice flow is weak everywhere it is westward between $x \sim 200$ and 500 km, but eastward elsewhere. Hence, along-shore convergence develops in the western portion of the model domain, while divergence occurs in the east. While numerical noise prevented more extensive analyses, these results, along with those from

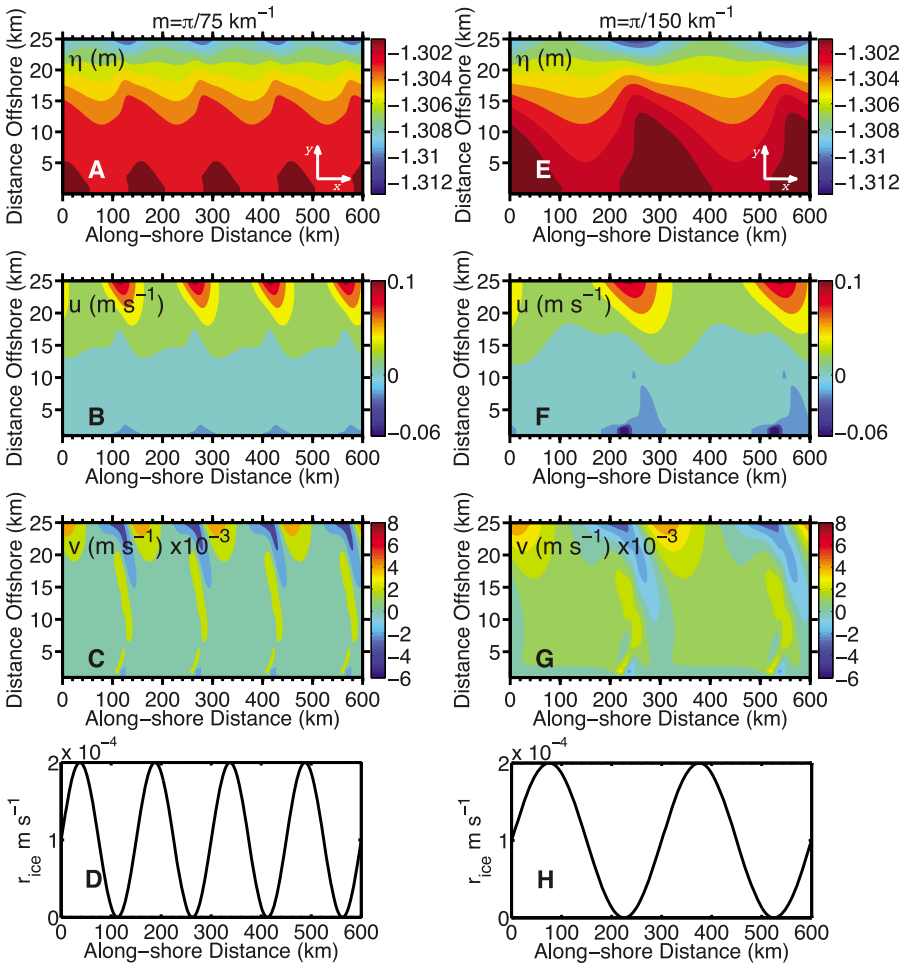

Figure 12. The effect of along-shore variations in r_{ice} on under-ice circulation. The along- and cross-shore distributions of (a) sea level anomaly, (b) vertically averaged u (positive velocities eastward), (c) vertically averaged v (positive velocities northward). (d) The along-shore distribution of r_{ice} for $r_{ice} = [10^{-2} + 10^{-2} \sin(mx)]10^{-2}$ with $m = \pi/75$ km^{-1}. (e–h) For $m = \pi/150$ km^{-1} and correspond to the legends for Figures 12a–12d.

section 3.4 and Figure 10, suggest that along-shore variations in ice width induce along-shore sea level slopes.

[52] We also examined the case for an along-shore domain of 2000 km in which there is no ice over the western edge of the domain ($x < 700$ km) but a 20 km-wide landfast ice cover for $x > 700$ km. (This situation mimics the ABS insofar as landfast ice terminates where the western boundary of this shelf joins the Chukchi Sea near Barrow, Alaska.) A spatially uniform 7 m s^{-1} westward wind is applied wherever ice is absent. To ensure that the results were not due to the asymmetries at the boundaries we tested three different configurations: (1) with ice/no ice/ice, (2) with no ice/ice/no ice, and (3) with no ice/ice. In the first two configurations the domain is periodic whereas in the third configuration, the

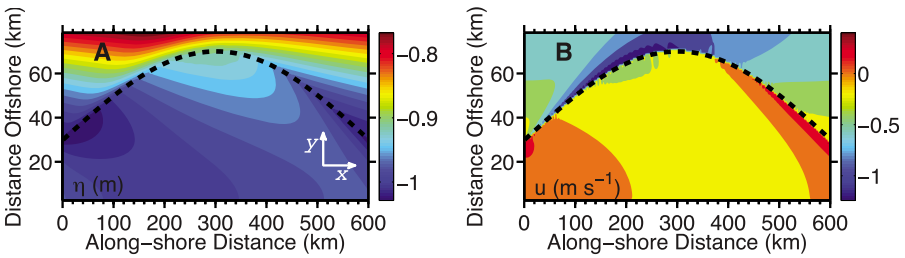

Figure 13. The effect of along-shore variations in the ice width on under-ice circulation. (a) Sea level anomaly from a linearized experiment with ice width increasing with along-shore distance. (b) Vertically averaged along-shore velocity. The ice edge is marked by the dashed line with ice covering the area inshore of the ice edge. A spatially uniform 7 m s^{-1} upwelling favorable wind is applied everywhere there is no ice.

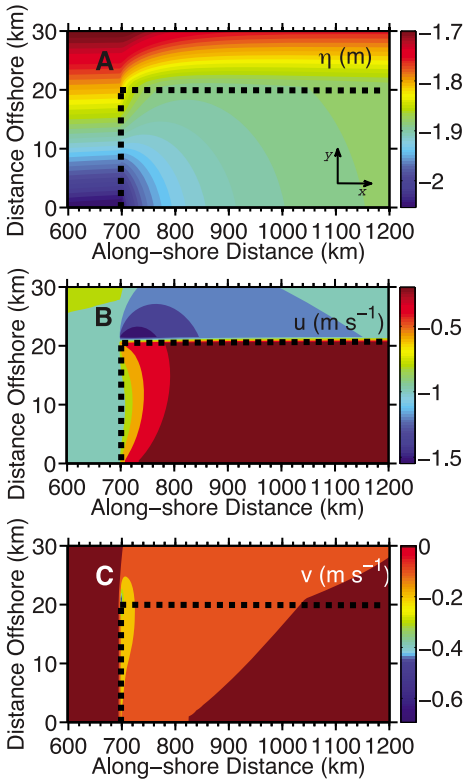

Figure 14. The effect of along-shore changes in ice coverage on under-ice circulation. The response after 10 days to a 7 m s^{-1} upwelling favorable (westward) wind stress blowing parallel to the ice edge at $y \geq 20$ km and $x > 700$ km and transverse to the landfast ice edge at $x < 700$ km. The ice edge is marked by the dashed line. (a) Sea level anomaly, (b) vertically averaged u (positive values indicate flow toward $+x$), and (c) vertically averaged v (positive values indicates flow toward +y).

domain is not periodic. As long as the domain was of sufficient length and sampling was done far from the boundaries, results were the same. The under-ice adjustment includes both a large, slowly varying and a smaller, but more rapidly varying response. The slowly varying response is illustrated after 10 days of forcing (with $r_{ice} = r_b = 10^{-4}$ m s^{-1}) in Figure 14. Upwelling develops along the western boundary of the landfast ice (denoted by the dashed line at $x = 700$ km) where coastal sea level is a minimum ($\eta \sim -2$ m). The westward winds applied over $x < 700$ km lead to a sea level depression at the western boundary of the landfast ice, which induces westward under-ice transport. In addition, $\partial\eta/\partial y > 0$ between the coast and the northern ice edge boundary (at $y = 20$ km). Recall, that $\partial\eta/\partial y < 0$ for the previous cases involving upwelling favorable winds seaward of the ice edge. In the present case $\partial\eta/\partial x$ is $\sim 5 \times 10^{-7}$ at $x = 800$ km and $\partial\eta/\partial y$ attains this value at $x = 1000$ km with both gradients diminishing to $O(10^{-8})$ by $x = 1200$ km. The vertically averaged along-shore velocity, u, (Figure 14b) decays rapidly to the east beneath the ice. For example, near the coast at $x \sim 700$ km (and west of the ice edge), u is ~ -1 m s^{-1}, but beneath the ice at $x = 800$ km u is westward and <0.10 m s^{-1}. For the constant r_{ice} case, the rapid decrease in the magnitude of u within ~ 100 km of the western boundary is similar to the decay scale found by KW for the case of a sea level mound imposed at the western boundary. By $x \sim 1100$ km (400 km east of the transverse ice edge), u is only ~ -0.01 m s^{-1} near the coast. Along-shore velocities are also ~ -0.01 m s^{-1} near the ice edge at $x \sim 1200$ km. Beneath the ice, the vertically averaged, cross-shore velocity (Figure 14c) is onshore as expected due to the westward transport.

[53] The more rapidly varying response includes topographic vorticity waves which are frictionally damped as they propagate eastward under the ice (Figure 15). The waves are generated by the abrupt surface stress curl at the western boundary of the landfast ice cover and recall the topographic waves generated at the edge of a storm [e.g., *McCreary and Chao*, 1985]. The waves propagate at ~ 1 m s^{-1} and have a wavelength and period of ~ 630 km and ~ 3.5 days. At the coast, the wave-induced $\partial\eta/\partial y$ is initially $\sim 10^{-7}$ and along-shore velocity fluctuations are 0.05 m s^{-1}. The waves' e-folding decay time scale is ~ 3.5 days and similar to the wave period.

4. Discussion and Conclusion

[54] Our results suggest that a spatially uniform upwelling-favorable wind blowing parallel to the edge of a landfast ice sheet of constant width over a linearly sloping bottom forces a coastal sea level set-down and a cross-shore sea level slope that drives an upwind geostrophic along-shore flow beneath the ice. The alongshore flow forces offshore transport in both the surface and bottom boundary layers, which can remove up to 15% of the under-ice volume over 10 days. The numerical experiments show that the cross-shore sea level slope and the time-dependent response of the circulation beneath the landfast ice depends upon both the magnitude and the cross-shore profile of r_{ice}, which determines the

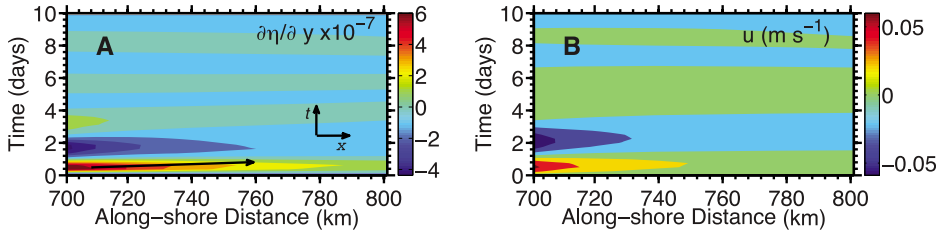

Figure 15. An under-ice vorticity wave. (a) The along-shore sea level slope at the coast as a function of along-shore distance and time and (b) the associated along-shore velocity variations. The black arrow in Figure 15a indicates the progression of the crest of the wave along the coast with time (and does not imply a velocity scale).

relative importance of the various vorticity tendencies. Increasing either r_{ice} or $\partial r_{ice}/\partial y$ (or both) decreases t_f and $|\partial\eta/\partial y|$ after 10 days. Increasing ice width increases both t_f and $|\partial\eta/\partial y|$. However, coastal sea level decreases less for a broad landfast ice zone compared to a narrower one.

[55] Partial observational support for this result comes from *Weingartner et al.*'s [2009] measurements from the ABS shelf. In early winter, as the landfast ice sheet formed, they observed a strong ($\sim$0.5 to 1 m s^{-1}) downwind, along-shore flow at the ice edge, but a weak ($<\sim$0.05 m s^{-1}) upwind flow beneath the landfast ice within a few kilometers of the ice edge. However, as winter progressed and the landfast ice edge expanded seaward, the relationship between winds and under-ice currents collapsed so that in general, there is no significant correlation between winds and under-ice currents. We suggest that along-shore variations in r_{ice} and/or landfast ice width are plausible mechanisms for the dissolution of this relationship. Both mechanisms can induce along-shore sea level slopes and under-ice currents that vary over spatial scales smaller than the length scale of the wind-forcing. If acting in tandem, both factors would further corrode any relationships between under-ice currents and winds. In addition we find that if the landfast ice edge terminates abruptly at its western boundary (as is the case for the ABS), the flow beneath the landfast ice is downwind for uniform upwelling-favorable along-shore winds. Given these various complications it is not surprising that there is no correlation between winds and under-ice currents in the landfast ice zone of the ABS. These same mechanisms should also conspire to degrade the along-shore coherence in currents beneath the landfast ice zone. Indeed, *Weingartner et al.* [2009] found that the along-shore coherence scales for sub-inertial, under-ice, along-shore currents is <200 km as opposed to coherence scales >300 km in ice-free conditions.

[56] Other mechanisms, not included in our simple models, may also erode the wind and under-ice current correlation. These include deep ice keels that block [*Macdonald and Carmack*, 1991] or channel the under-ice flow and/or variations in ice thickness that influence the water depth (and thus vortex stretching). Moreover, we have treated the landfast ice edge as an abrupt boundary, offshore of which the flow is driven by a uniform surface wind stress. In fact, 3-day repeat satellite image analyses of ice motion by *Morris et al.* [1999] from the East Siberian Sea suggest there is a transition zone between the landfast and freely drifting ice. Within this transition zone, internal ice stresses are likely important. These stresses should reduce, but not eliminate, the efficacy of momentum transfer between the atmosphere and ocean. A transition zone would further alter the spatial variability in r_{ice} and thus the effective ice width.

[57] *Weingartner et al.* [2009] measured nearshore sea level fluctuations beneath the ABS landfast ice of 0.5 m or more during winter. Our results suggest that changes in sea level develop due to cross-shore transports within the under-ice and bottom boundary layers. In the case of uniform along-shore conditions, these boundary layer transports are not compensated for by a cross-shore interior flow. Consequently, under such conditions circulation beneath the landfast ice will take a long time to reach the steady state of no under-ice flow described by equation (4). Hence, relatively large fluctuations in sea level may occur, which may lead to "breakout events" (in which sections of the landfast ice detach from shore and begin drifting (C. George and H. Eicken, personal communication, 2010). These events will change the surface stress distribution and, by exposing nearshore waters to the atmosphere, promote ice growth and dense water formation.

[58] Finally, *Weingartner et al.* [2009] observed sea level fluctuations that propagated eastward with a period of $\sim$4 days, a phase speed of $\sim$1 m s^{-1} and a wavelength of $\sim$900 km. The under-ice current fluctuations associated with these features are $\sim$0.03 m s^{-1}. These disturbances may reflect slope processes [*Aagaard and Roach*, 1990; *Pickart et al.*, 2011], but they may also be initiated by winds blowing transverse to the western boundary of the landfast ice zone (see section 3.7).

[59] The idealized modeling approach adopted here explored how circulation in the landfast ice zone may evolve in response to wind-forcing. We invoked simple (and perhaps naïve) ideas on variations in ice-ocean frictional coupling and ice width within the landfast ice zone. Our results suggest that temporal and spatial gradients in these parameters induce cross- and along-shore pressure gradients that drive the under-ice circulation and degrade the wind-current correlation. The ice parameters change seasonally and synoptically due to landfast ice expansion (or reduction due to breakouts) and deformation processes within and along the edge of the landfast ice zone. The models and observations imply that landfast ice dynamics, not explicitly included herein, may effectively convert the long-wavelength forcing of the wind into shorter-scale ocean motions beneath the landfast ice.

Appendix A

[60] We begin with the time-dependent vertically averaged momentum equations [e.g., *Kundu and Cohen*, 2008].

$$\begin{aligned}\frac{\partial u}{\partial t} - fv &= -g\frac{\partial \eta}{\partial x} - B_x - S_x + F\\ \frac{\partial v}{\partial t} + fu &= -g\frac{\partial \eta}{\partial y} - B_y - S_y\\ \frac{\partial (uh)}{\partial x} + \frac{\partial (vh)}{\partial y} &= -\frac{\partial \eta}{\partial t}\end{aligned} \tag{A1}$$

where u and v are the along- and cross-shore velocities (m s^{-1}), respectively, g is the acceleration due to gravity (m s^{-2}), η is the sea level anomaly (m), h is the depth ($h = sy$, m), B and S are the surface and bottom stresses due to bottom and under-ice friction, respectively, and F is the wind stress. Note that B and S both have the same sign.

[61] Assuming that B and S are proportional to the under-ice geostrophic transport, we have

$$\begin{aligned}\frac{\partial u}{\partial t} - fv &= -g\frac{\partial \eta}{\partial x} - \frac{(r_{ice} + r_b)u}{h} + F\\ \frac{\partial v}{\partial t} + fu &= -g\frac{\partial \eta}{\partial y} - \frac{(r_{ice} + r_b)v}{h}\\ \frac{\partial (uh)}{\partial x} + \frac{\partial (vh)}{\partial y} &= -\frac{\partial \eta}{\partial t}\end{aligned} \tag{A2}$$

where r_{ice} (m s^{-1}) is the linear under-ice friction coefficient, $r_{ice} = r_{ice}(x,y)$, and r_b (m s^{-1}) is the linear bottom friction coefficient.

[62] Multiplying the momentum equations by h and then taking the curl (noting that F is zero everywhere under the ice) leads to a time-dependent, under-ice vorticity equation:

$$\frac{\partial \eta}{\partial x} = \underbrace{\frac{\partial}{\partial t}\left\{\frac{1}{sf}\left[\frac{\partial}{\partial x}\left(h\frac{\partial \eta}{\partial x}\right) - \frac{\partial}{\partial y}\left(h\frac{\partial \eta}{\partial y}\right)\right] - \frac{f}{sg}\eta\right\}}_{\text{Time variation in relative vorticity and stretching}} + \underbrace{\frac{1}{sf}\left[\frac{\partial (r_{ice}+r_b)}{\partial y}\frac{\partial \eta}{\partial y} + \frac{\partial (r_{ice}+r_b)}{\partial x}\frac{\partial \eta}{\partial x}\right]}_{\text{Frictional Curl term}} + \underbrace{\frac{(r_{ice}+r_b)}{sf}\left(\frac{\partial^2 \eta}{\partial y^2} + \frac{\partial^2 \eta}{\partial x^2}\right)}_{\text{Relative Vorticity}} . \tag{A3}$$

In the absence of along-shore variations, (A3) can be re-written as:

$$\underbrace{\frac{\partial}{\partial t}\left[\frac{1}{sf}\frac{\partial}{\partial y}\left(h\frac{\partial \eta}{\partial y}\right) + \frac{f}{sg}\eta\right]}_{\substack{\text{Time variation in relative vorticity,} \\ \text{Term 3, and stretching}}} = \underbrace{\frac{1}{sf}\frac{\partial}{\partial y}\left[(r_{ice}+r_b)\frac{\partial \eta}{\partial y}\right]}_{\text{Terms 1 \& 2}} \tag{A4}$$

from which we see that term 3, the time rate of change of the relative vorticity i.e., under-ice vorticity generation, tends to buffer the frictional curl and the relative vorticity (terms 1 and 2). At steady state equation (A4) reduces to the ALW vorticity equation, equation (2) in the text.

[63] A further useful diagnostic equation can be derived from the steady state form of (A2). Taking the curl of the steady state governing equations leads to:

$$\underbrace{\frac{\partial \eta}{\partial x}}_{\substack{\text{Along Shore} \\ \text{Sea Level} \\ \text{Slope}}} = \frac{1}{gs}\left[\underbrace{(r_b v)_x - (r_b u)_y}_{\text{Bottom Stress Curl}} + \underbrace{(r_{ice} v)_x - (r_{ice} u)_y}_{\text{Surface Stress Curl}} - \underbrace{(F_y)_x - (F_x)_y}_{\text{Wind Stress Curl}}\right] \tag{A5}$$

which shows that the along-shore sea level slope is balanced by the stress curls divided by the bottom slope. This is text equation (6) after omitting the wind stress curl terms.

[64] **Acknowledgments.** K. Hedstrom, R. Gradinger, M. Johnson, and Z. Kowalik provided helpful comments. J.K. was supported by the Prince William Sound Oil Spill Recovery Institute (OSRI), Alaska Sea Grant in cooperation with the Center for Global Change and the UAF Graduate School. Additional support was provided to J.K. and T.W. by the U.S. BOEMRE through the University of Alaska Coastal Marine Institute (Contract 1435-01-02-CA-85294) and by the Office of Naval Research through the National Oceanographic Partnership Program (grant N00014-07-1-1040). The Arctic Region Supercomputing Center (ARSC) generously provided the computing resources for the numerical experiments.

References

Aagaard, K., and A. T. Roach (1990), Arctic ocean-shelf exchange: Measurements in Barrow Canyon, *J. Geophys. Res.*, *95*(C10), 18,163–18,175, doi:10.1029/JC095iC10p18163.

Arakawa, A., and V. R. Lamb (1977), *Methods of Computational Physics*, Academic, San Diego, Calif.

Clarke, A. J. (1978), On wind-driven quasi-geostrophic water movements at fast ice edges, *Deep Sea Res.*, *25*(1), 41–47.

Csanady, G. T. (1978), The arrested topographic wave, *J. Phys. Oceanogr.*, *8*(1), 47–62, doi:10.1175/1520-0485(1978)008<0047:TATW>2.0.CO;2.

Csanady, G. T. (1981), Shelf circulation cells, *Philos. Trans. R. Soc. A*, *302*(1472), 515–530, doi:10.1098/rsta.1981.0180.

Danielson, S., and M. Johnson (2008), Alaskan waters 1 km gridded bathymetry based on ship soundings, paper presented at the Alaska Marine Science Symposium (AMSS), AMSS, Anchorage, Alaska, 20–23 January.

Fennel, W., and O. M. Johannessen (1998), Wind forced oceanic responses near ice edges revisited, *J. Mar. Syst.*, *14*(1–2), 57–79, doi:10.1016/S0924-7963(97)00018-3.

Gammelsrod, T., M. Mork, and L. P. Roed (1975), Upwelling possibilities at an ice edge: A homogeneous model, *Mar. Sci. Commun.*, *1*(2), 115–145.

Gill, A. E., and E. H. Schumann (1974), The generation of long shelf waves by the wind, *J. Phys. Oceanogr.*, *4*(1), 83–90, doi:10.1175/1520-0485(1974)004<0083:TGOLSW>2.0.CO;2.

Kundu, P. K., and I. M. Cohen (2008), *Fluid Mechanics*, 4th ed., xxviii + 872 pp., Academic, Amsterdam.

Lu, P., Z. Li, C. Bin, and M. Leppäranta (2011), A parameterization of the ice-ocean drag coefficient, *J. Geophys. Res.*, *116*, C07019, doi:10.1029/2010JC006878.

Macdonald, R. W., and E. C. Carmack (1991), The role of large-scale under-ice topography in separating estuary and ocean on an Arctic shelf, *Atmos. Ocean*, *29*(1), 37–53, doi:10.1080/07055900.1991.9649391.

Mahoney, A., H. Eicken, and L. Shapiro (2007), How fast is landfast sea ice? A study of the attachment and detachment of nearshore ice at Barrow, Alaska, *Cold Reg. Sci. Technol.*, *47*(3), 233–255, doi:10.1016/j.coldregions.2006.09.005.

McCreary, J. P., and S.-Y. Chao (1985), Three-dimensional shelf circulation along an eastern ocean boundary, *J. Mar. Res.*, *43*(1), 13–36, doi:10.1357/002224085788437316.

McPhee, M. G. (1990), Small scale processes, in *Polar Oceanography, Part A: Physical Science*, edited by W. C. Smith, pp. 287–334, Academic, San Diego, Calif.

Mellor, G. L., and T. Yamada (1982), Development of a turbulence closure model for geophysical fluid problems, *Rev. Geophys.*, *20*(4), 851–875, doi:10.1029/RG020i004p00851.

Morris, K., S. Li, and M. Jefferies (1999), Meso- and microscale sea-ice motion in the East Siberian Sea as determined from ERS-1 SAR data, *J. Glaciol.*, *45*(15), 370–383, doi:10.3189/002214399793377239.

Pickart, R. S., G. W. K. Moore, D. J. Torres, P. S. Fratantoni, R. A. Goldsmith, and J. Yang (2009), Upwelling on the continental slope of the Alaskan Beaufort Sea: Storms, ice, and oceanographic response, *J. Geophys. Res.*, *114*(C1), C00A13, doi:10.1029/2008JC005009.

Pickart, R. S., M. A. Spall, G. W. K. Moore, T. J. Weingartner, R. A. Woodgate, K. Aagaard, and K. Shimada (2011), Upwelling in the Alaskan Beaufort Sea: Atmospheric forcing and local versus non-local response, *Prog. Oceanogr.*, *88*(1–4), 78–100, doi:10.1016/j.pocean.2010.11.005.

Shchepetkin, A. F., and J. C. McWilliams (2005), The regional oceanic modeling system (ROMS): A split-explicit, free-surface, topography-following-coordinate oceanic model, *Ocean Modell.*, *9*(4), 347–404, doi:10.1016/j.ocemod.2004.08.002.

Shirasawa, K. (1986), Water stress and ocean current measurements under first-year sea ice in the Canadian Arctic, *J. Geophys. Res.*, *91*(C12), 14,305–14,316, doi:10.1029/JC091iC12p14305.

Song, Y. T., and D. Haidvogel (1994), A semi-implicit ocean circulation model using a generalized topography-following coordinate system, *J. Comput. Phys.*, *115*(1), 228–244, doi:10.1006/jcph.1994.1189.

Song, Y. T., and D. G. Wright (1998), A general pressure gradient formulation for ocean models: Part II. Energy, momentum, and bottom torque consistency, *Mon. Weather Rev.*, *126*(12), 3231–3247, doi:10.1175/1520-0493(1998)126<3231:AGPGFF>2.0.CO;2.

Tucker, W. B., III, W. F. Weeks, and M. Frank (1979), Sea ice ridging over the Alaskan continental shelf, *J. Geophys. Res.*, *84*(C8), 4885–4897, doi:10.1029/JC084iC08p04885.

Weingartner, T. J., S. L. Danielson, J. L. Kasper, and S. R. Okkonen (2009), Circulation and water property variations in the nearshore Alaskan Beaufort Sea (1999–2007), report, 154 pp., Miner. Manage. Serv., U.S. Dep. of the Interior, Anchorage, Alaska.

J. L. Kasper, Department of Physical Oceanography, Woods Hole Oceanographic Institution, 266 Woods Hole Rd., MS 21, Woods Hole, MA 02543, USA. (jkasper@whoi.edu)

T. J. Weingartner, Institute of Marine Science, University of Alaska Fairbanks, PO Box 757220, Fairbanks, AK 99775, USA.